

Article

# Influence of Chloride Ions on Electrochemical Corrosion Behavior of Dual-Phase Steel over Conventional Rebar in Pore Solution

Hany S. Abdo <sup>1,2</sup> , Asiful H. Sheikh <sup>1,\*</sup> , Jabair A. Mohammed <sup>1</sup> , Monis Luqman <sup>3</sup>,  
Sameh A. Ragab <sup>1</sup> and Saud M. Almotairy <sup>1</sup> 

<sup>1</sup> Centre of Excellence for Research in Engineering Materials, King Saud University, P.O. Box 800, Riyadh 11421, Saudi Arabia; habdo@ksu.edu.sa (H.S.A.); jmohammed@ksu.edu.sa (J.A.M.); sragab@ksu.edu.sa (S.A.R.); salmotairy1@ksu.edu.sa (S.M.A.)

<sup>2</sup> Mechanical Design and Materials Department, Faculty of Energy Engineering, Aswan University, Aswan 81521, Egypt

<sup>3</sup> Mechanical Engineering Department, College of Engineering, King Saud University, P.O. Box 800, Riyadh 11421, Saudi Arabia; monisluqman9@gmail.com

\* Correspondence: aseikh@ksu.edu.sa

Received: 16 May 2020; Accepted: 19 June 2020; Published: 30 June 2020



**Abstract:** Reinforced steel bars (rebar) are extensively used in construction, and the main challenge is in minimizing corrosion due to oxide or passive layer breakdown. In contrast, dual-phase (DP) steel has good corrosion resistance. This study investigated the effect of  $\text{Cl}^-$  ions on the electrochemical corrosion behavior of DP rebar and conventional rebar. Corrosion behavior studies and electrochemical measurements were conducted on DP rebar and conventional rebar in simulated concrete pore solution with different concentrations of  $\text{Cl}^-$  ions. Microstructure analysis, surface morphology analysis, and corroded surface characterization were performed using optical microscopy, field emission scanning electron microscopy, and Raman spectroscopy, respectively. Potentiodynamic polarization and electrochemical impedance spectroscopy measurements revealed that DP rebar has good passivity, leading to better corrosion resistance and greater strength compared to ordinary rebar. In addition, DP rebar showed better passivity behavior compared to conventional rebar in alkaline solution. Therefore, the presence of a dual phase (ferrite and martensite) in reinforced concrete structured steel induces good corrosion resistance.

**Keywords:** dual phase steel; rebar; microstructure; annealing; electrochemical properties

## 1. Introduction

Because of their durability and versatility, reinforced steel bars (rebar) are extensively used in construction. However, corrosion of rebar leads to cracks and spalling on the surface, affecting the safety and durability of reinforced concrete. The main challenge for conventional rebar is how to minimize corrosion due to oxide or passive layer breakdown. The apprehension about chloride-induced corrosion has motivated researchers to focus on carbon materials, such as carbon steel, as reinforcement for concrete. To calculate the required chloride percentage for passivation, three methods are used: the total chloride amount in weight percent (wt. %), the free chloride concentration ( $\text{Cl}^-$ ), and the chloride/hydroxide ( $\text{Cl}/\text{OH}$ ) ratio [1]. In addition, different methods are used to measure the chloride content percentage, such as electrochemical impedance, potentiodynamic polarization, gravimetric measurement [2–11].

Failure of the oxide or passive layer is usually due to the reaction of  $\text{Cl}^-$  ions with the rebar surface in an appropriate alkaline environment [12–16]. Various experiments have been conducted

to understand the relationship between corrosion rate and Cl% in the environment surrounding rebar reinforcing concrete, especially under alkaline conditions [17–22], in order to optimize the different conditions and generate a susceptible Cl% suitable for pitting. Studies have reported that Cl% varies depending on many parameters. Li and Sagues [16] showed that the critical Cl% is between 0.01 and 0.04 M in saturated calcium hydroxide and 0.4–0.6 M in simulated concrete pore solution (SCPS-PH-13.5). Bertolini et al. [18] reported a relationship between the critical Cl% of carbon steel and the solution pH, and Cl% increased from 0.17 M at pH 12.5 to >0.27 M at pH 13.8 in sodium hydroxide solution.

The mechanical performance, reliability, and durability of the rebar surface are significantly affected by its corrosion behavior. Alonso et al. [17] described how mechanical properties are affected by pitting corrosion on the rebar surface. A pitting morphology leads to stress concentration, initiating cracks and fatigue failure due to crack propagation. Therefore, analyzing the corrosion behavior of pits is important for estimating the life of reinforced concrete structures [20].

In non-cracked concrete, corrosion of reinforced steel starts from the high-concentration chloride area via an anodic localized reaction. In cracked concrete, corrosion of reinforced steel starts from the area where small anodes formed around the crack line [18]. In active corrosion, macro- and microcell corrosion can exist simultaneously [19]. Many factors affect the corrosion of reinforced steel in cracked concrete, such as concrete composition and resistance, loading, and exposure conditions [20,23].

The dual-phase (DP) steel microstructure is characterized by a matrix of fine ferrite with S.M.A. II spots of a second, harder phase—high-strength steel. Although some of bainite or retained austenite might be present, the second phase mainly comprises martensite. The martensite volume fraction ranges between 5% and 30%. Martensite offers significant strengthening, while the ductile ferrite matrix offers good formability [24–26]. DP rebar acquires its mechanical properties from the two phases [27–33], and the presence of a dual phase in reinforced concrete structured steel induces good corrosion resistance.

Many variables affect the ductility of an element while it is subjected to different loads, especially a bending moment, such as the element material, cross-sectional geometry, and mechanical properties. Especially, for reinforced concrete, these variables are represented by strength, the concrete's mechanical properties, reinforcement ductility, bonding between reinforcement and concrete, cross-sectional geometry, structural details, transverse shear and longitudinal force, and element slenderness. Intercritical quenching (IQP) is an effective method of improving the ferrite–martensite structure by enhancing the density of mobile dislocations and increasing residual stresses.

This study investigated the effect of Cl<sup>-</sup> ions on the electrochemical corrosion behavior of DP rebar over conventional rebar in SCPS.

## 2. Materials and Methods

### 2.1. Heat Treatment

A DP structure was produced from low-carbon steel via two heat treatment steps, as shown in Figure 1. Step 1 was a normalizing process for 60 min at 950 °C in a tube furnace, and Step 2 was an annealing process for 75 min at 770 °C before quenching in ice-brine water at an average temperature of −10 °C.

### 2.2. Metallography

To investigate the microstructure, we cut out samples from the as-received rebar using a Struers Secotom-10 saw. Grinding was performed using silicon carbide paper with different grades (320–2500). Next, fine polishing was performed using a SPECTRUM SYSTEM™ 1000 automatic fine polisher with ferrous alumina as a lubricant in order to obtain a smooth surface without scratches. The samples surfaces were washed with distilled water (DW) and carefully cleaned twice with ethanol to get a polished mirror surface. Finally, etching was performed, where the polished surface was

immersed in 2% nital solution for 8 s to get a clear grain boundary view, and microstructure images were taken using a Leica DM 2500M optical microscope (Leica Camera, Wetzlar, Germany). The SEM images were acquired using a Carl Zeiss ultra 55 Field-Emission Scanning Electron Microscope operated at 5 kV.

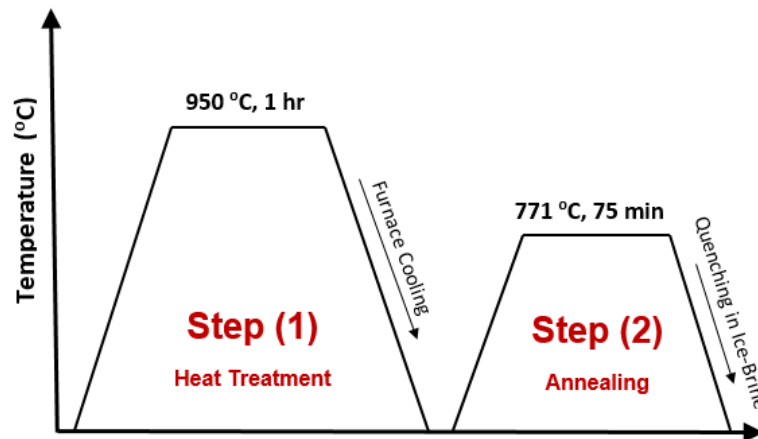


**Figure 1.** Heat treatment of dual phase (DP) rebar.

### 2.3. Hardness

Vickers hardness was measured for both rebar and DP rebar using a Vickers Buehler-Micro-Met 5114 Microhardness Tester (Akashi Corporation, Tokyo, Japan) with an applied load of 100 g for 10 s. The hardness values reported were the average of five different positions per sample.

### 2.4. Volume Fraction

The martensite volume fraction for DP rebar was calculated via image processing using a Leica material workstation software (Leica Microsystems, Wetzlar, Germany). To obtain statistically reliable results, images of etched surfaces were taken at different magnifications from at least 10 positions, and the average volume fraction was calculated.

### 2.5. Corrosion

The SCPS used was the same as described previously [16]. The authors investigated the SCPS chemistry of alkali-activated fly ash and found that the percentage of dissolved elements, such as Ca, Al, P, and Si, was in the range of 0.5–1 mM. To simulate SCPS chemistry, we used an alkali hydroxide solution: NaOH solution was prepared with a concentration of 0.80 M using ACS reagent-grade sodium hydroxide pellets, and 0.02 and 0.05 M sodium chloride was added to study the effect of Cl<sup>-</sup> ions on corrosion initiation.

Electrochemical impedance spectroscopy (EIS) and potentiodynamic polarization were used to study corrosion performance using a three-electrode potentiostat device. Briefly, 1 cm<sup>2</sup> from each sample as an exposed surface mounted with epoxy resin was considered the working electrode, while the saturated calomel electrode (SCE) was the reference electrode, and a graphite rod was the counter-electrode. To prepare the sample surface for microstructure imaging, the same preparation steps were used as in Section 2.2. After fine polishing and washing (with acetone and DW), samples were immersed for 30 min in the electrolyte for stabilization and to steady the open-circuit potential before each experiment. EIS was performed over a wide frequency range (100 kHz to 0.01 Hz), and polarization curves were obtained at a potential of −1000 to +1200 mV (SCE) with a constant scan rate of 1 mV/s.

### 3. Results and Discussion

#### 3.1. Microstructure

Figure 2 and Table 1 show the as-received rebar microstructure. It comprised two phases, a ferrite phase (white regions) and a pearlite phase (dark regions). The grains were oriented in a random direction, and we observed homogeneous distribution of the two phases in the microstructure.

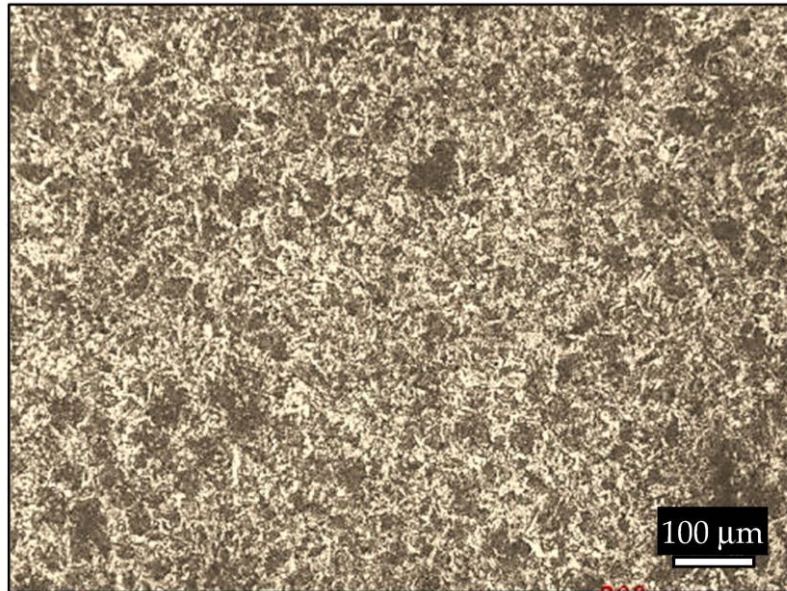


**Figure 2.** Microstructure of the as-received rebar.

**Table 1.** Nominal composition of (a) carbon steel and (b) DP steel in (wt %).

(a)								(b)				
C	Mn	Si	S	P	V	Mo	Nb	C	Mn	Si	S	P
0.20	0.70	0.172	0.027	0.020	<0.02	<0.02	<0.01	0.10	0.90	0.30	0.010	0.02

Figure 3 shows the DP rebar microstructure. It also comprised two phases, a soft ferrite phase (white regions) and a hard martensite phase (dark regions). The grains looked larger compared to rebar and were oriented in a random direction. We determined the relative amount of ferrite and martensite via image processing using Leica LS image analyzer software. The martensite volume fraction was almost equal to the area fraction because the sample was thin (900 mm), which came to ~22% in DP rebar.

#### 3.2. Hardness

The average hardness values for conventional rebar and DP rebar samples were 257 and 310 VHN, respectively. Hardness measurements were obtained from five indentations in different areas per sample.

#### 3.3. Potentiodynamic Polarization

##### 3.3.1. Influence of $\text{Cl}^-$ ions on Passivity in Alkaline Solution

Figure 4 shows potentiodynamic polarization curves for SCPS with and without NaCl. As explained by Pourbaix diagram [34], DP rebar shows spontaneous passivity in the presence of an alkaline medium compared to conventional rebar. High  $\text{Cl}^-$  ion concentrations may affect the passive state [35].

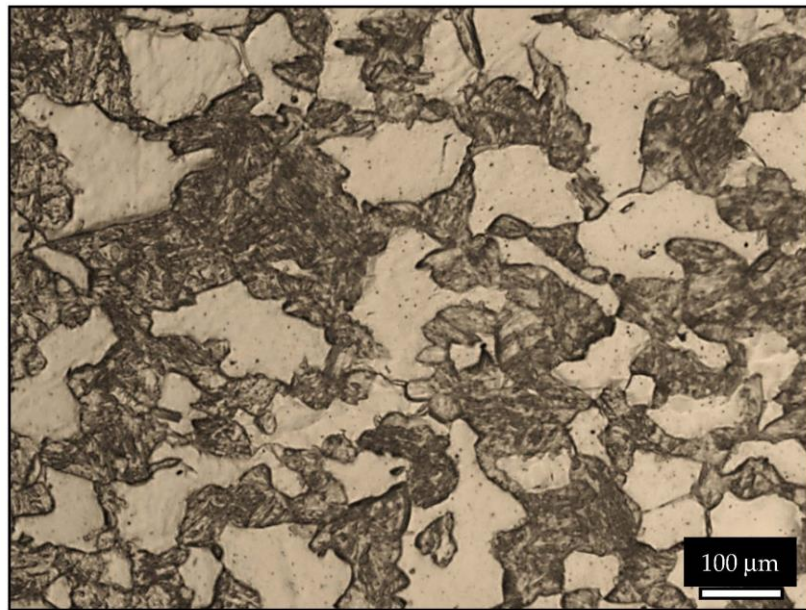


Figure 3. Microstructure of DP rebar produced by heat treatment.

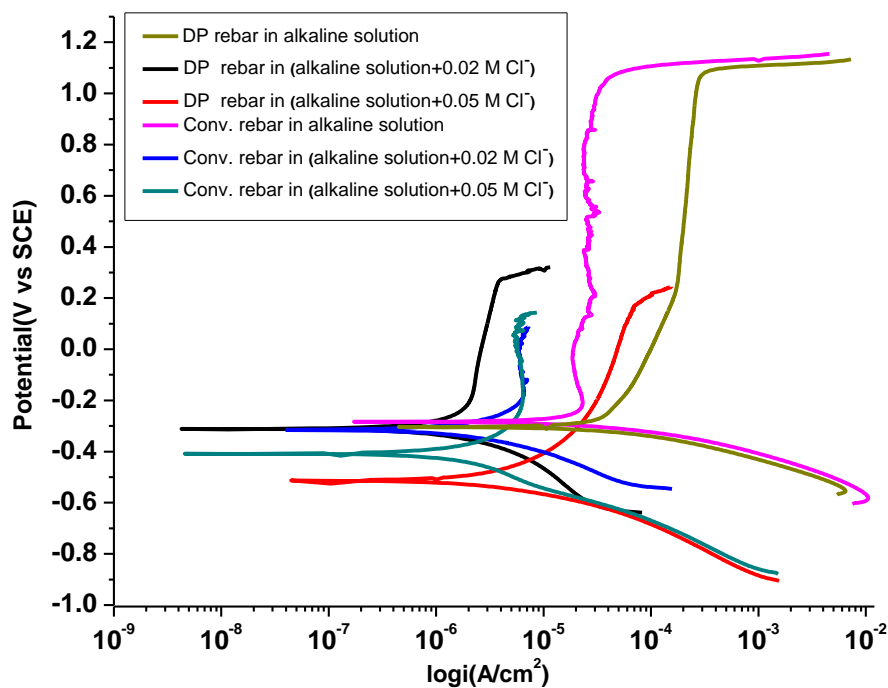


Figure 4. Potentiodynamic polarization curves in simulated concrete pore solution (SCPS) with and without NaCl. SCPS, simulated concrete pore solution.

We observed oxide or passive layer breakdown at  $\text{Cl}^-$  ion concentrations of 0.02 and 0.05 M and potential of  $>200$  mV (SCE). The higher  $\text{Cl}^-$  ion concentration shifts the critical pitting potential toward a less noble range, as seen at 0.05 M. It is well known that among different factors contributing to the initiation of pitting corrosion is the damage to passive layer. Moreover, pitting corrosions limits the possibility of re-passivation leading to complete destruction of the oxide layer. In other words, the lower the destruction in the passive layer the better the corrosion resistant property of the material. Thus, it can be confirmed that DP rebar has a better corrosion resistance than the conventional rebar.

This is clearly seen from the behaviour of these materials as depicted in Figure 4 where the dissolution rate of the passive layer in the DP rebar is far slower than that of conventional rebar.

Sodium chloride was added to the base electrolyte prior to potentiodynamic polarization, which helped in investigating the susceptibility of the oxide or passive layer formed in the local breakthrough. Low  $\text{Cl}^-$  ion concentrations are instrumental in preventing the formation of a protective layer on substrates [36]. The oxide or passive layer dissolves actively with high current densities beginning at the free corrosion potential, which is shown for a  $\text{Cl}^-$  ion concentration of 0.05 M for conventional rebar and DP rebar in Figure 4. At all solution concentrations, the corrosion rate was higher for conventional rebar compared to DP rebar, probably because the oxide or passive layer of DP rebar was more stable compared to conventional rebar. By increasing the  $\text{Cl}^-$  ion concentration, the free corrosion and passive current densities increased, while the free corrosion potential decreased to a less noble potential. Because of an increase in surface reactivity for conventional rebar in SCPS with increasing  $\text{Cl}^-$  ion concentration (0.02 and 0.05 M), we observed current scattering increasing in the current anodic range with high passive current density. The reason was the presence of an oxide or passive layer during anodic polarization, which dissolved and reformed dynamically. At 200 mV (SCE), the current density rapidly increased by 2 orders of magnitude. Oxygen evolution reaction was not the only reason for this increase, because on decreasing the applied potential, the current density did not decrease [37]. Oxide or passive layer breakthrough was evident from the formation of high quantities of flakes on the electrode surface.

### 3.3.2. Oxide or Passive Layer Breakdown Mechanism and Pit Morphology

Figure 5a,b shows the surface morphology of conventional rebar and DP rebar after oxide or passive layer breakdown during anodic polarization in SCPS containing NaCl. The surface morphologies showing pitting on the surface seemed different, although the electrolyte composition used was the same. We observed cracks beside the pits formed by corrosion. In addition, we observed cracks initiating oxide or passive layer breakthrough at other places. Hydrogen absorption at the metal surface might be possible. Water molecules or hydrogen ions might get reduced at the metal surface and seep through the broken oxide or passive layer, facilitating hydrogen absorption, which might form hydrides [34,38]. This generates tensile stress, leading to crack initiation in the oxide or passive layer. Cracking inhibits repassivation and promotes active dissolution. Anodic dissolution and crack propagation are responsible for the growth of pits in the vertical (depth) and lateral directions, respectively.

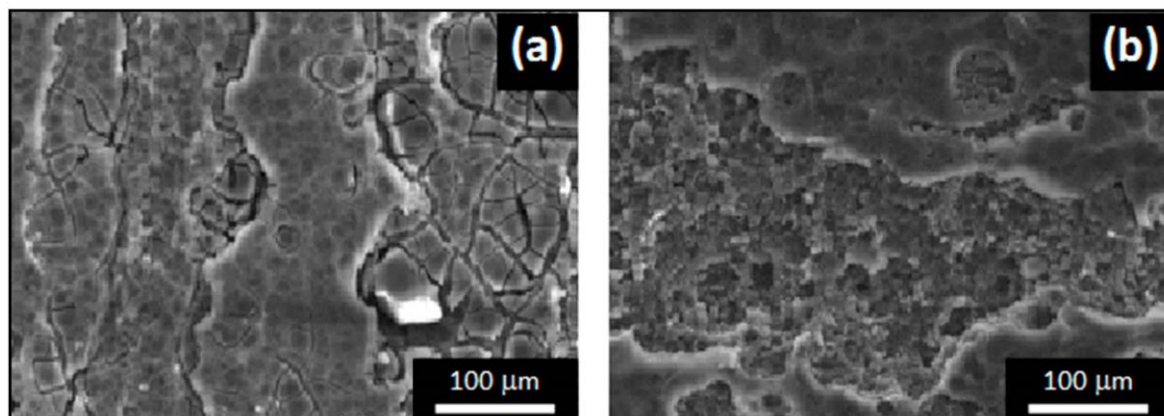


**Figure 5.** Surface morphology of (a) conventional rebar and (b) DP rebar.

We also observed unprompted passivity for DP rebar in alkaline solution with  $\text{Cl}^-$  ions, which was stable under anodic polarization.  $\text{Cl}^-$  ions showed a stronger effect, and alkaline layers revealed a

greater steadiness for DP rebar. High  $\text{Cl}^-$  ion concentrations in a strongly alkaline solution can induce breakdown of DP rebar passivity.

### 3.4. Electrochemical Impedance Spectroscopy

EIS results at 0 V (SCE) showed that diffusion controls oxide or passive layer growth in conventional rebar and DP rebar. Figure 6 shows the equivalent circuit, where  $Q$  is the constant phase element CPE,  $R_s$  the solution resistance,  $W$  the Warburg impedance, and  $R_t$  the layer transition resistance. According to diffusion boundary conditions, there are three types of diffusion impedances for plane electrodes [39,40].

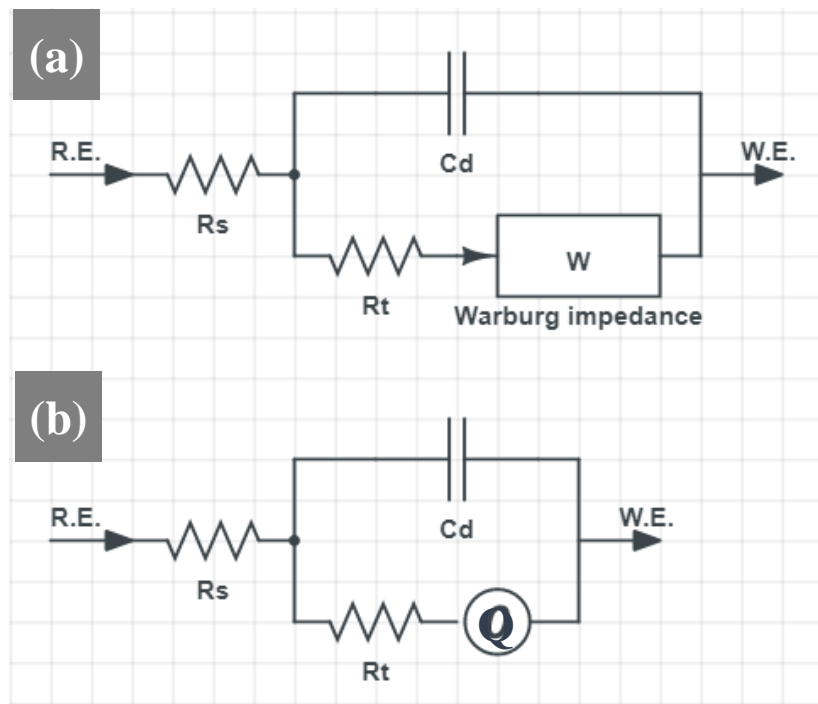


**Figure 6.** Equivalent circuit impedance for (a) conventional rebar, and (b) DP rebar. Rebar, reinforced steel bars; DP, dual phase.

Warburg impedance, one of the common diffusion impedances, assumes the infinity diffusion layer thickness. This equivalent circuit impedance can be expressed as follows:

$$Z_F = R_s + Z_F^0 + Z_w, \tag{1}$$

where  $Z_F^0$  the Faraday impedance and  $Z_w$  the Warburg impedance.  $Z_F^0$  and  $Z_w$  are expressed as follows:

$$Z_F^0 = R_t, \tag{2}$$

$$Z_w = \frac{\gamma R_t |I_F|}{nFC_s \sqrt{2\omega D}} (1 - j), \tag{3}$$

where  $I_F$  the Faraday current,  $\gamma$  the series of the reactant in the electrode reaction,  $\omega$  the sine potential frequency,  $n$  the chemical coefficient of electrode,  $F$  the Faraday constant, and  $D$  the diffusion coefficient.

When the Warburg impedance controls the electrode reaction, impedance is expressed as follows:

$$Z_F = R_s + R_t + \frac{\gamma R_t |I_F|}{nFC_s \sqrt{2\omega D}} (1 - j) \tag{4}$$

The second impedance is represented by cotangent hyperbolic (O) diffusion, and the impedance ( $Z_F$ ) is expressed as follows:

$$Z_F = R_s + Z_F^0 + Z_d = R_s + R_t \left( 1 + \frac{\gamma |I_F| I}{n F C_s D} \right) \quad (5)$$

where  $Q$  is the magnitude of admittance of the constant phase element CPE and  $n$  is the CPE exponent. The  $n$  value refers to the phase shift and can characterize different surface phenomena such as surface heterogeneity (inhomogeneity) resulting from surface roughness, dissolution of the metal, impurities, distribution of the active sites, or porous layer formation. The value of the coefficient ( $n$ ) gives the frequency dependence.

Limiting values of the coefficient ( $n$ ) are zero for a pure resistor and one for an ideal capacitor. Intermediate values of ( $n$ ) indicate imperfect capacitive behavior and a CPE with ( $n = 0.5$ ) usually referred to a Warburg Element, where  $\chi^2$  gives the overall regression coefficient for the fit.

The interfacial charge transfer resistance  $R_t$  and the double layer capacitance  $C_d$  are the key parameters characterizing the passive behavior of ductile iron, while higher  $R_t$  and lower  $C_d$  on the surface of ductile iron results is meaning better corrosion resistance.

Figures 7–9 show Nyquist planes for the above two diffusion elements. Experimental EIS spectra of conventional rebar and DP rebar are shown in Figure 7. For DP rebar, the Nyquist plot indicates hyperbolic diffusion, which existed only in the passive process. In contrast, conventional rebar diffusion changed from the Warburg impedance ( $W$ ) to a high-frequency capacitive loop.

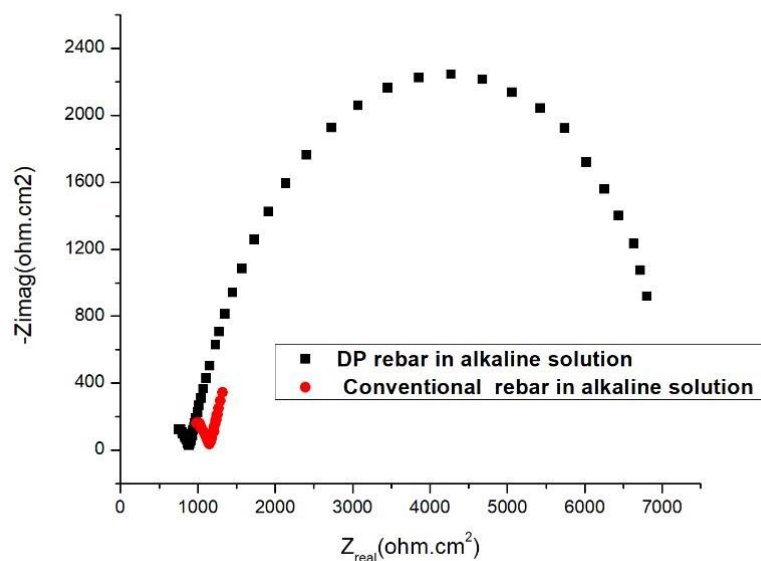


**Figure 7.** Electrochemical impedance spectroscopy (EIS) Nyquist curve in an alkaline solution (without  $\text{Cl}^-$  ions). EIS, electrochemical impedance spectroscopy.

All parameters of potentiodynamic polarization and EIS results in an alkaline solution with and without different  $\text{Cl}^-$  ion concentrations are listed in Table 2. The polarization resistance ( $R_t$ ) for the DP rebar oxide or passive layer was larger compared to conventional rebar. This result also verified that the passive current density of DP rebar is lower compared to conventional rebar as concluded from Figures 8 and 9.

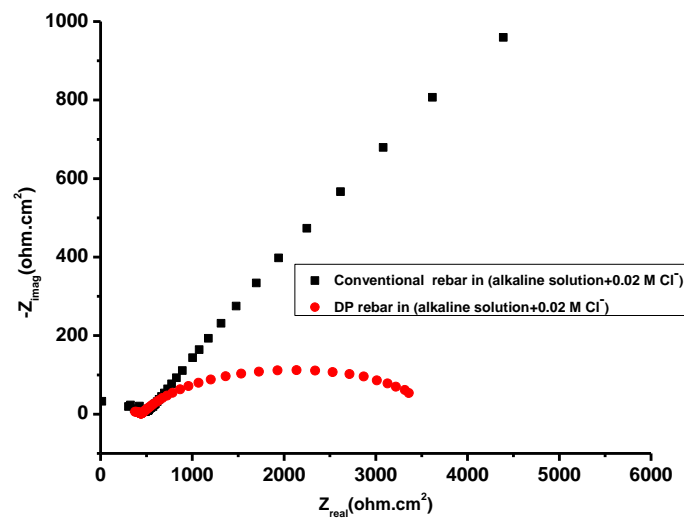


**Figure 8.** EIS Nyquist curve in an alkaline solution +0.02 M Cl<sup>-</sup> ions. EIS, electrochemical impedance spectroscopy.

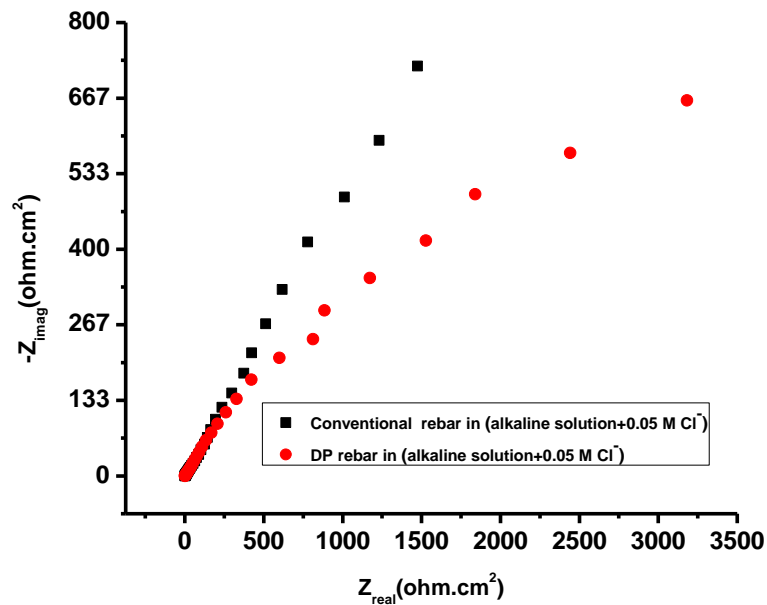


**Figure 9.** EIS Nyquist curve in an alkaline solution +0.05 M Cl<sup>-</sup> ions. EIS, electrochemical impedance spectroscopy.

**Table 2.** Potentiodynamic polarization and EIS results in an alkaline solution with and without different Cl<sup>-</sup> ion concentrations.

Material	Solution	$i_{corr}$ (A/cm <sup>2</sup> ) μA	$E_{corr}$ (mv) (V vs. SCE)	$\beta_c$ (V/decade)	$\beta_a$ (V/decade)	$R_{ii}$ (ohm cm <sup>2</sup> ) × 10 <sup>-6</sup>	$R_p$ (ohm cm <sup>2</sup> )	$C_{dl} \times 10^{-4}$ (F cm <sup>2</sup> )	$\chi^2$ , Chi-Squared × 10 <sup>-2</sup>
DP steel	Alkaline	12	-294	0.151	0.140	132	7000	7.24	3.142
Rebar		25	-300	0.159	0.148	154	6100	8.45	3.876
DP steel	Alkaline +0.02 M Cl <sup>-</sup>	80	-304	0.168	0.156	160	3600	9.26	3.768
Rebar		104	-310	0.170	0.162	172	300	10.89	4.181
DP steel	Alkaline +0.05M Cl <sup>-</sup>	102	-400	0.180	0.172	183	2800	11.98	4.251
Rebar		143	-550	0.192	0.180	190	2260	14.10	4.166

### 3.5. Capacitance

The oxide or passive layer formed on metals significantly affects corrosion resistance [41]. The layer usually exhibits semiconducting properties [42,43]. The most common technique for investigating the electronic properties of an oxide or passive layer is Mott–Schottky plot measurement, which characterizes the oxide or passive layer generated on metal surfaces. In this study, we used electrochemical capacitance measurements to characterize the electron properties of the oxide or passive layer formed on conventional rebar and DP rebar.

Capacitance  $C$  is equal to the space charge capacitance  $C_{sc}$ . Referring to the Mott–Schottky principle, the relation between  $1/C^2$  and potential  $E$  can be written as follows [43]:

$$\frac{1}{C^2} = \frac{2}{\epsilon \epsilon_0 q N A^2} \left( -E + E_{fb} + \frac{kT}{e} \right) \tag{6}$$

where  $q$  is the electron charge,  $E_{fb}$  the flat band potential,  $\epsilon_0$  the vacuum permittivity,  $\epsilon$  the dielectric constant,  $T$  the absolute temperature,  $k$  the Boltzmann constant,  $A$  the electrode area and  $N$  the carrier concentration. We can calculate the semiconductor type from the  $V$  versus  $1/C^2$  plot. A p-type semiconductor can be detected from the negative slope, while an n-type semiconductor is associated with the positive slope of the oxide or passive layer.

Figure 10 shows the Mott–Schottky plot of the oxide or passive layers for conventional rebar and DP rebar. The positive slopes obtained were associated with n-type semiconductors of the oxide or passive layer of both conventional rebar and DP rebar. Specifically, the rebar phase did not affect or change the semiconductor type. The slope of the  $V$  versus  $1/C^2$  plot was contrariwise relational to the carrier concentration. The slope of DP rebar was larger compared to conventional rebar, indicating that the donor concentration in the oxide or passive layer of DP rebar is lower compared to conventional rebar.  $N_d$  was obtained from the slopes:  $1.67 \times 10^{22} \text{ cm}^{-3}$  for conventional rebar and  $9.07 \times 10^{20} \text{ cm}^{-3}$  for DP rebar.

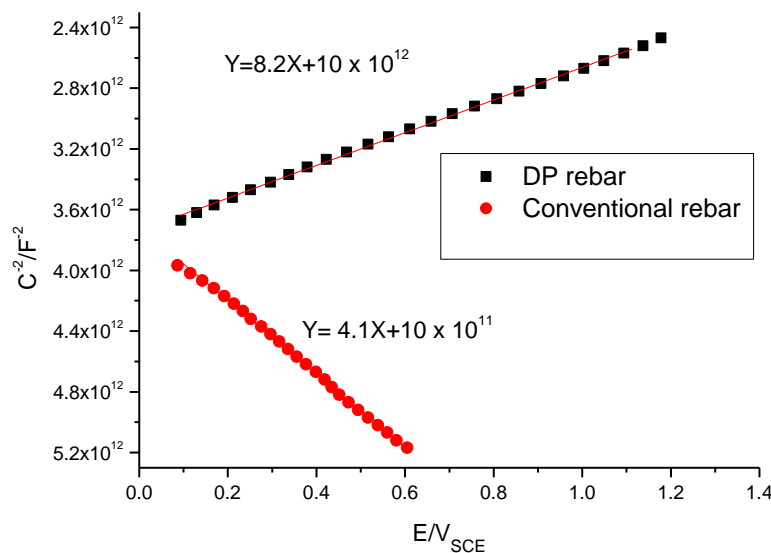


Figure 10. Mott–Schottky plot of DP rebar and conventional rebar.

EIS results showed that passive layer formation of conventional rebar and DP rebar was diffusion controlled. During passive layer formation, the electrochemical stage is faster than the diffusion stage. The electrochemical stage is activated at the layer–metal interface, where metal ionization occurs. Oxygen vacancies or metal ions predominate in the oxide or passive layer because of a rapid electrochemical process. The oxide or passive layer is an n-type semiconductor, so the oxide or passive layers of conventional rebar and DP rebar are n-type semiconductors. The EF of the electrode decreases

if anode polarization is applied to the passive electrode, which bends the energy band upward to the side of the electrolyte.

In conventional rebar, the electron ( $e^-$ ) originated from the conductive range in the oxide or passive layer, which resulted in increasing the magnitude of  $N_d$ . The more the donors the oxide or passive layer has, the easier the anodic reaction process is. In addition, the passive current density for conventional rebar is larger compared to DP rebar. The main conclusion is that in conventional rebar, an inner layer from pearlite oxide is formed in the oxide or passive layer, increasing the passive current density and forming an unstable oxide or passive layer.

As it can be seen from Table 2, the current density is becoming higher with increasing chlorine percentage but increasing rate higher in case of conventional rebar compare to DP steel, which is in accordance with the values of  $E_{corr}$ . For the present study, the polarization curves are important because the anodic and cathodic slopes  $\beta_a$  and  $\beta_c$  were determined to be used in the calculation of corrosion rates. The Tafel regions in the polarization curves are well defined. Especially,  $\beta_a$  and the Tafel slopes were the largest values, indicating that the diffusion of the specimens can have an influence on the rate-controlling step, whereas Tafel slopes with larger values  $\beta_c$  are typical for systems, which are not purely activation, or diffusion controlled which will be associated to oxygen diffusion. In general, the cathodic curves pattern in all solution indicated the reduction reactions of both: hydrogen ions and oxygen.

### 3.6. Raman Spectroscopy

The rust compositions for conventional rebar and DP rebar were determined using Raman spectroscopy. The main products were oxyhydroxides or iron oxides, which represent the corrosion products of conventional rebar used for reinforcing construction cement. The composition of rust is iron (Fe) and iron oxide ( $Fe_3O_4$ ). Low oxygen availability and the restricting concrete surrounding are the main reasons for  $Fe_3O_4$  formation. Iron chloride ( $FeCl_2$ ) is generated because of the chloride augmented layer. The comparatively low-intensity peaks of  $FeCl_2$  might be due to the thin  $FeCl_2$  layer. In some regions, the  $Fe_3O_4$ ,  $\gamma$ - $FeOOH$ , and  $\alpha$ - $FeOOH$  formation indicates more oxidation, which might contribute to the cracking characteristics of the rust formed. There is a greater probability of  $\gamma$ - $Fe_2O_3$  formation because of additional crystallization and dehydration at higher oxygen levels in external areas.

Raman spectroscopy helps in determining the composition of steel surfaces and hence corrosion behavior. Figure 11 shows in situ Raman spectra for reinforcing steel submerged in SCPS (saturated  $Ca(OH)_2$  solution) with and without NaCl. The wide peak close to  $1650\text{ cm}^{-1}$  clearly showed the bending vibration of  $H_2O$  in SCPS [44]. In addition, the peaks at  $277$  and  $713\text{ cm}^{-1}$  belonged to  $\gamma$ - $Fe_2O_3$  and  $\alpha$ - $Fe_2O_3$ , respectively [45,46]. Steel can maintain passivity in chloride-free SCPS. In addition, the oxide or passive layer deposition (restoration) and dissolution occur all together in dynamic steadiness on the steel surface [47].

In this study, oxide or passive layer dissolution formed  $Fe^{2+}$  at the SCPS–steel interface, indicating that in chloride-free SCPS, there is no reaction because of the absence of  $Fe^{2+}$ , while in SCPS containing chloride, more  $Fe^{2+}$  ions are produced to react with SCPS for the same duration.

For conventional rebar, the  $Fe_2O_3$  Raman spectrum became more intense, displaying acceleration or oxide or passive film dissolution because of the chloride effect, confirmed by electrochemical studies. The low-intensity peaks at  $722$  and  $282\text{ cm}^{-1}$  showed  $\gamma$ - $Fe_2O_3$  and  $\alpha$ - $Fe_2O_3$ , respectively (Figure 12) [48,49]. Subsequently,  $\gamma$ - $Fe_2O_3$  and  $\alpha$ - $Fe_2O_3$  could be measured, compared to chloride-free SCPS, and were identified to be constituting the upper surface layer of steel [50,51].

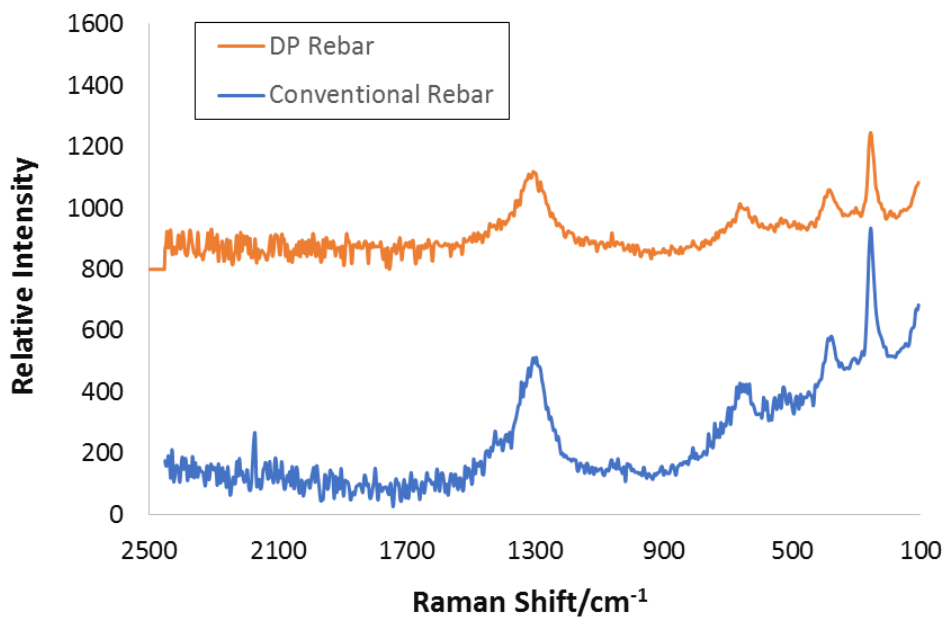


**Figure 11.** Raman spectroscopy images in an alkaline solution after potentiodynamic polarization.

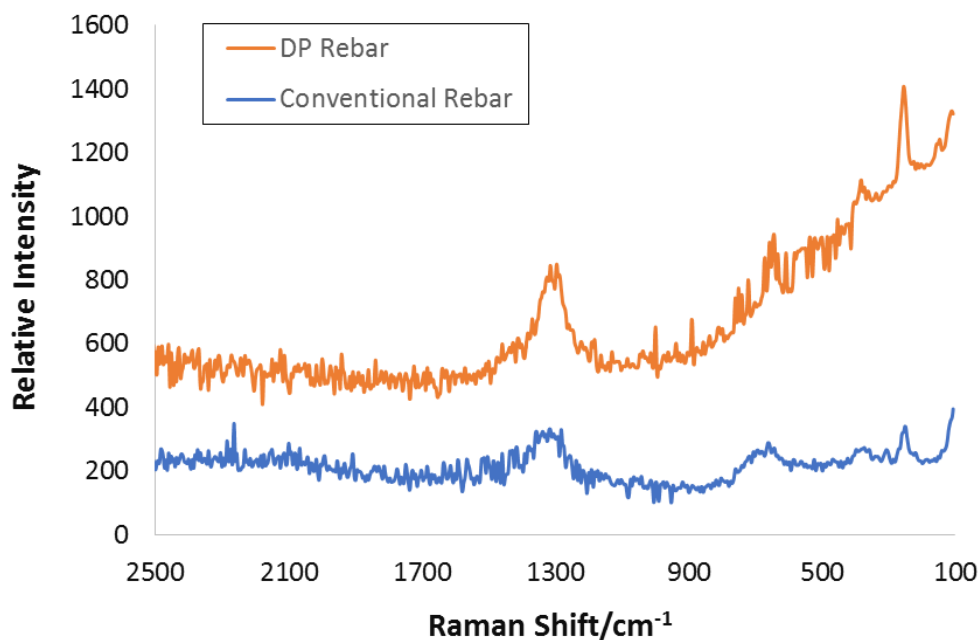


**Figure 12.** Raman spectroscopy images in alkaline and Cl<sup>-</sup> solutions after potentiodynamic polarization.

### 3.7. Scanning Electron Microscopy

The bowl shape is the favored spot for pit nucleation, and it represents pitting growth initiation locations. The bowl shape takes a downward concave form because of gravity and its effect on electrolyte streaming, and it is the shortest path for mass transportation. In this study, an increase in time broadened the pit concave, and Fe(II) cations were formed generated because of Cl<sup>-</sup> ions flowing into the widening pit. These Fe(II) cations are the main reason for charge neutrality in the spot location. Scanning electron microscopy (SEM) image topography showed a pearlite phase in the deepest area all over the concave spot, indicating the aggressive effect of pearlite toward pit progression. Anion and cation vacancies at the chloride–metal interface form voids in the pit (Figure 13). If these vacancies penetrate the metal phase at a slower rate compared to their transference through the layer, it would

accumulate at the chloride–metal interface [52,53]. Pitting is often responsible for the high concentration of ions, which may promote pit depth [52].

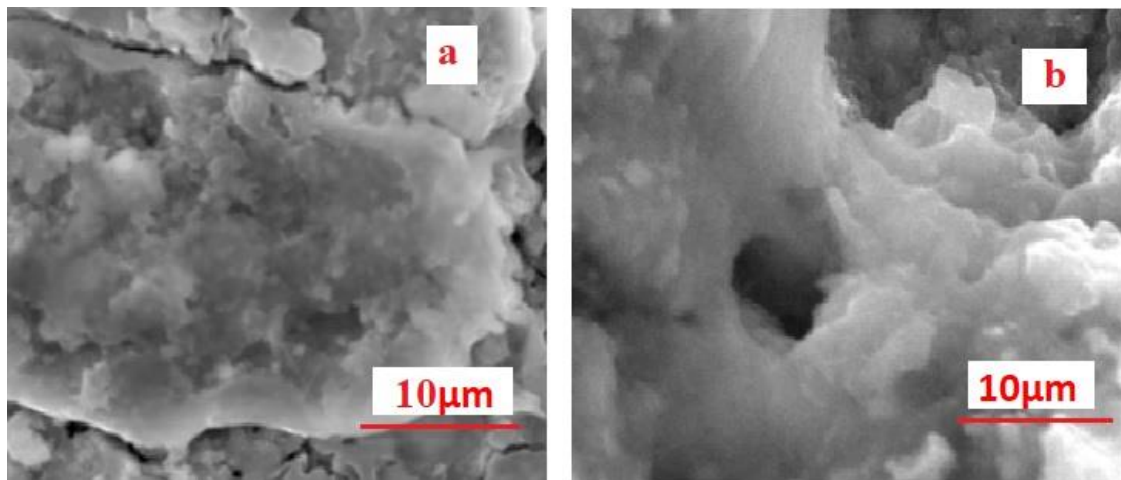


**Figure 13.** SEM images after potentiodynamic polarization of (a) DP rebar and (b) conventional rebar.

Energy dispersive X-ray (EDS) analysis technique were conducted along with SEM examination to identify the elements in the oxide layers of the different samples. The results of the EDS spectra are shown in Figure 14. The atomic percentage content of iron, chlorine and oxygen representative data are presented graphically in Figure 14a conventional rebar and Figure 14b for DP rebar. The predominant elements detected on all samples were Fe and O. Trace amounts of Mn, S and Si were also detected. It is not possible to obtain quantitative compositional information from EDS analyses. However, qualitative or at best semi quantitative information can be derived from a careful comparison of the peak energy heights of the different elements. Thus, considering the peak heights of Fe and O in Figure 14b indicates that presence of Fe oxide, most likely in the form of  $\text{Fe}_2\text{O}_3$  or  $\text{Fe}_3\text{O}_4$  is higher in case of DP steel compared to non-conventional rebar.

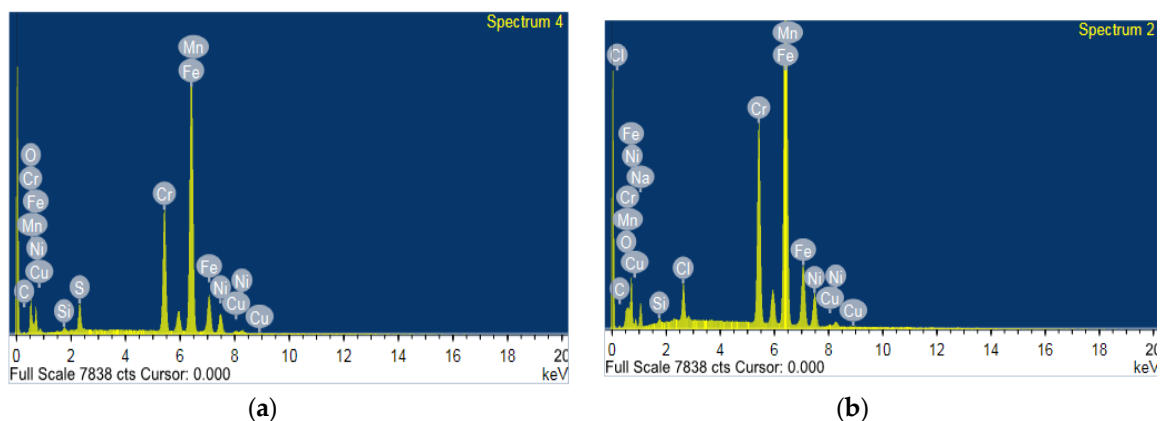


**Figure 14.** Energy dispersive X-ray (EDS) analysis after potentiodynamic polarization of (a) conventional rebar and (b) DP rebar.

#### 4. Conclusions

DP rebar has a higher pitting potential compared to conventional rebar in SCPS. DP rebar forms more stable products compared to conventional rebar. Conventional rebar has more pitting density compared to DP rebar. We successfully developed a high-performance DP rebar microstructure from low-carbon steel through heat treatment. DP rebar has good passivity properties, which lead to better corrosion resistance and greater strength compared to conventional rebar.

**Author Contributions:** Conceptualization, H.S.A. and A.H.S.; methodology, A.H.S. and H.S.A.; software, J.A.M. and S.M.A.; validation, M.L. and S.M.A.; formal analysis, S.A.R.; investigation, H.S.A. and A.H.S.; resources, A.H.S.; data curation, J.A.M. and S.M.A.; writing—original draft preparation, H.S.A. and A.H.S.; writing—review and editing, H.S.A.; supervision, A.H.S.; project administration, H.S.A.; funding acquisition, A.H.S. All authors have read and agreed to the published version of the manuscript.

**Funding:** This research received no external funding.

**Acknowledgments:** The authors would like to extend their sincere appreciation to the Deanship of Scientific Research at King Saud University for its funding of this research through the Research Group Project No. RG-1439-029.

**Conflicts of Interest:** The authors declare no conflicts of interest.

## References

1. Alonso, C.; Andrade, C.; Castellote, M.; Castro, P. Chloride threshold values to depassivate reinforcing bars embedded in a standardized OPC mortar. *Cem. Concr. Res.* **2000**, *30*, 1047–1055. [[CrossRef](#)]
2. Kayyali, O.A.; Haque, M.N. The  $\text{Cl}^-/\text{OH}^-$  ratio in chloride-contaminated concrete—A most important criterion. *Mag. Concr. Res.* **1995**, *47*, 235–242. [[CrossRef](#)]
3. Raupach, M. Chloride-induced macrocell corrosion of steel in concrete—Theoretical background and practical consequences. *Constr. Build. Mater.* **1996**, *10*, 329–338. [[CrossRef](#)]
4. Thomas, M. Chloride thresholds in marine concrete. *Cem. Concr. Res.* **1996**, *26*, 513–519. [[CrossRef](#)]
5. Melchers, R.E.; Li, C.Q. Reinforcement corrosion initiation and activation times in concrete structures exposed to severe marine environments. *Cem. Concr. Res.* **2009**, *39*, 1068–1076. [[CrossRef](#)]
6. Lambert, P.; Page, C.L.; Vassie, P.R.W. Investigations of reinforcement corrosion. 2. Electrochemical monitoring of steel in chloride-contaminated concrete. *Mater. Struct.* **1991**, *24*, 351–358. [[CrossRef](#)]
7. Gouda, V.K.; Shater, M.A. ChemInform Abstract: Corrosion inhibition of reinforcing steel by using hydrazine hydrate. *Chem. Informationsd.* **1975**, *6*. [[CrossRef](#)]
8. Bouteiller, V.; Cremona, C.; Baroghel-Bouny, V.; Maloula, A. Corrosion initiation of reinforced concretes based on Portland or GGBS cements: Chloride contents and electrochemical characterizations versus time. *Cem. Concr. Res.* **2012**, *42*, 1456–1467. [[CrossRef](#)]
9. Hansson, C.M.; Sorensen, B. Threshold concentration of chloride in concrete for the initiation of reinforcement corrosion. *ASTM Spec. Tech. Publ.* **1990**, *19*, 3–16.
10. Mangat, P.S.; Molloy, B.T. Factors influencing chloride-induced corrosion of reinforcement in concrete. *Mater. Struct.* **1992**, *25*, 404–411. [[CrossRef](#)]
11. Almusallam, A.A. Effect of degree of corrosion on the properties of reinforcing steel bars. *Constr. Build. Mater.* **2001**, *15*, 361–368. [[CrossRef](#)]
12. Goñi, S.; Andrade, C. Synthetic concrete pore solution chemistry and rebar corrosion rate in the presence of chlorides. *Cem. Concr. Res.* **1990**, *20*, 525–539. [[CrossRef](#)]
13. Hansson, C.M. Corrosion of Reinforcing Bars in Concrete. *ACI J. Proc.* **1965**, *62*. [[CrossRef](#)]
14. Glass, G.K.; Buenfeld, N.R. The influence of chloride binding on the chloride induced corrosion risk in reinforced concrete. *Corros. Sci.* **2000**, *42*, 329–344. [[CrossRef](#)]
15. Andrade, C.; Page, C.L. Pore solution chemistry and corrosion in hydrated cement systems containing chloride salts: A study of cation specific effects. *Br. Corros. J.* **1986**, *21*, 49–54. [[CrossRef](#)]
16. Li, L.; Sagüés, A.A. Effect of chloride concentration on the pitting and repassivation potentials of reinforcing steel in alkaline solutions. In Proceedings of the NACE—International Corrosion Conference Series, San Antonio, Texas, USA, 25–30 April 1999; p. 19.
17. Alonso, C.; Castellote, M.; Andrade, C. Chloride threshold dependence of pitting potential of reinforcements. *Electrochim. Acta* **2002**, *47*, 3469–3481. [[CrossRef](#)]
18. Bertolini, L.; Bolzoni, F.; Pastore, T.; Pedferri, P. Behaviour of stainless steel in simulated concrete pore solution. *Br. Corros. J.* **1996**, *31*, 218–222. [[CrossRef](#)]
19. Schießl, P.; Raupach, M. Laboratory Studies and Calculations on the Influence of Crack Width on Chloride-Induced Corrosion of Steel in Concrete. *ACI Mater. J.* **1997**, *94*. [[CrossRef](#)]
20. Andrade, C.; Maribona, I.R.; Feliu, S.; González, J.A.; Feliu, S. The effect of macrocells between active and passive areas of steel reinforcements. *Corros. Sci.* **1992**, *33*, 237–249. [[CrossRef](#)]

21. Andrade, C.; Merino, P.; Nóvoa, X.R.; Pérez, M.C.; Soler, L. Passivation of Reinforcing Steel in Concrete. *Mater. Sci. Forum* **1995**, *192*, 891–898. [[CrossRef](#)]
22. Moser, R.D.; Singh, P.M.; Kahn, L.F.; Kurtis, K.E. Chloride-induced corrosion resistance of high-strength stainless steels in simulated alkaline and carbonated concrete pore solutions. *Corros. Sci.* **2012**, *57*, 241–253. [[CrossRef](#)]
23. Li, C.Q.; Yang, S.T. Prediction of Concrete Crack Width under Combined Reinforcement Corrosion and Applied Load. *J. Eng. Mech.* **2011**, *137*, 722–731. [[CrossRef](#)]
24. Blunt, J.; Jen, G.; Ostertag, C.P. Enhancing corrosion resistance of reinforced concrete structures with hybrid fiber reinforced concrete. *Corros. Sci.* **2015**, *92*, 182–191. [[CrossRef](#)]
25. Dieter, G.E. *Mechanical Metallurgy*; McGraw-Hill: New York, NY, USA, 1961.
26. Galán, J.; Samek, L.; Verleysen, P.; Verbeken, K.; Houbaert, Y. Advanced high strength steels for automotive industry. *Rev. Metal.* **2012**, *48*, 118–131. [[CrossRef](#)]
27. Mintz, B. Hot dip galvanising of transformation induced plasticity and other intercritically annealed steels. *Int. Mater. Rev.* **2001**, *46*, 169–197. [[CrossRef](#)]
28. Bleck, W.; Phiu-On, K. Microalloying of cold-formable multi phase steel grades. *Mater. Sci. Forum* **2005**, *500*, 97–114. [[CrossRef](#)]
29. Ball, A.; Chauhan, Y.; Schaffer, G.B. Microstructure, phase equilibria, and transformations in corrosion resistant dual phase steel designated 3CR12. *Mater. Sci. Technol.* **1987**, *3*, 189–196. [[CrossRef](#)]
30. Verdeja, J.I.; Pero-Sanz, J.A.; Asensio, J. Multiphase Steels: Structure-Mechanical Properties Relationships in the Cold Rolled and Continuous Annealed Condition. *Mater. Sci. Forum* **2005**, *500–501*, 429–436. [[CrossRef](#)]
31. Byers, H.G.; Langdon, S.C. Passivity of Metals. *J. Am. Chem. Soc.* **1914**, *36*, 2004–2011. [[CrossRef](#)]
32. Bode, R.; Meurer, M.; Schaumann, T.W.; Warnecke, W. Selection and use of coated advanced high-strength steels for automotive applications. *Rev. Métallurgie* **2004**, *101*, 551–558. [[CrossRef](#)]
33. Zackay, V.; Parker, E.R.; Fahr, D.; Busch, R. The enhancement of ductility in high-strength steels. *Trans. ASM* **1967**, *60*, 252–259.
34. Parsons, R. Atlas of electrochemical equilibria in aqueous solutions. *J. Electroanal. Chem. Interfacial Electrochem.* **1967**, *13*, 471. [[CrossRef](#)]
35. Galvele, J.R. Effect of Molybdenum on the Pitting Potential of High Purity 18% Cr Ferritic Stainless Steels. *J. Electrochem. Soc.* **1978**, *125*, 1204. [[CrossRef](#)]
36. Park, S.A.; Kim, S.H.; Yoo, Y.H.; Kim, J.G. Effect of chloride ions on the corrosion behavior of low-alloy steel containing copper and antimony in sulfuric acid solution. *Met. Mater. Int.* **2015**, *21*, 470–478. [[CrossRef](#)]
37. Mao, X.; Liu, X.; Revie, R.W. Pitting Corrosion of Pipeline Steel in Dilute Bicarbonate Solution with Chloride Ions. *Corrosion* **1994**, *50*, 651–657. [[CrossRef](#)]
38. El-Moneim, A.; Gebert, A.; Uhlemann, M.; Gutfleisch, O.; Schultz, L. The influence of Co and Ga additions on the corrosion behavior of nanocrystalline NdFeB magnets. *Corros. Sci.* **2002**, *44*, 1857–1874. [[CrossRef](#)]
39. González-Cortés, A. Electrochemical Impedance Spectroscopy. In *Agricultural and Food Electroanalysis*; John Wiley & Sons, Ltd.: Chichester, UK, 2015; pp. 381–419. ISBN 9781118684030.
40. Orazem, M.E.; Tribollet, B. *Electrochemical Impedance Spectroscopy*; John Wiley & Sons, Inc.: Hoboken, NJ, USA, 2008; ISBN 9780470381588.
41. Cicek, V. *Corrosion Engineering*; John Wiley & Sons, Inc.: Hoboken, NJ, USA, 2014; ISBN 9781118720837.
42. Leidheiser, H. Electrochemistry at semiconductor and oxidized metal electrodes. *J. Colloid Interface Sci.* **1982**, *88*, 310. [[CrossRef](#)]
43. Sato, N. *Electrochemistry at Metal and Semiconductor Electrodes*; Elsevier: Amsterdam, The Netherlands, 1998; ISBN 9780444828064.
44. John, N.; George, S. Raman Spectroscopy. In *Spectroscopic Methods for Nanomaterials Characterization*; Elsevier: Amsterdam, The Netherlands, 2017; pp. 95–127. ISBN 9780323461467.
45. Baek, W.C.; Kang, T.; Sohn, H.J.; Kho, Y.T. In situ surface enhanced Raman spectroscopic study on the effect of dissolved oxygen on the corrosion film on low carbon steel in 0.01 M NaCl solution. *Electrochim. Acta* **2001**, *46*, 2321–2325. [[CrossRef](#)]
46. Ohtsuka, T.; Kubo, K.; Sato, N. Raman Spectroscopy of Thin Corrosion Films on Iron at 100 to 150 C in Air. *Corrosion* **1986**, *42*, 476–481. [[CrossRef](#)]
47. Otto, A.; Bruckbauer, A.; Chen, Y. On the chloride activation in SERS and single molecule SERS. *J. Mol. Struct.* **2003**, *661*, 501–514. [[CrossRef](#)]

48. Li, Y.S.; Li, J.C.; Cheng, Y.W. Surface-enhanced raman spectra of dyes and organic acids in silver solutions: Chloride ion effect. *Spectrochim. Acta Part A Mol. Biomol. Spectrosc.* **2003**, *56A*, 2067.
49. Kumar, V. Protection of Steel Reinforcement for Concrete—A Review. *Corros. Rev.* **1998**, *16*. [[CrossRef](#)]
50. Koleva, D.A.; de Wit, J.H.W.; van Breugel, K.; Lodhi, Z.F.; van Westing, E. Investigation of Corrosion and Cathodic Protection in Reinforced Concrete. *J. Electrochem. Soc.* **2007**, *154*, 52. [[CrossRef](#)]
51. Ryan, M.P.; Williams, D.E.; Chater, R.J.; Hutton, B.M.; McPhail, D.S. Why stainless steel corrodes. *Nature* **2002**, *415*, 770–774. [[CrossRef](#)] [[PubMed](#)]
52. Ke, R. Initiation of Corrosion Pits at Inclusions on 304 Stainless Steel. *J. Electrochem. Soc.* **1995**, *142*, 4056. [[CrossRef](#)]
53. Punckt, C. Sudden Onset of Pitting Corrosion on Stainless Steel as a Critical Phenomenon. *Science* **2004**, *305*, 1133–1136. [[CrossRef](#)] [[PubMed](#)]



© 2020 by the authors. Licensee MDPI, Basel, Switzerland. This article is an open access article distributed under the terms and conditions of the Creative Commons Attribution (CC BY) license (<http://creativecommons.org/licenses/by/4.0/>).